Simulation study of the effects of buildings, trees and paved surfaces on ambient dose equivalent rates outdoors at three suburban sites near Fukushima Dai-ichi

Minsik Kim[1*], Alex Malins[1], Kazuya Yoshimura[2], Kazuyuki Sakuma[2,3], Hiroshi Kurikami[1,3], Akihiro Kitamura[1,3], Masahiko Machida[1], Yukihiro Hasegawa[4], Hideaki Yanagi[4]

[1] Japan Atomic Energy Agency, Center for Computational Science and e-Systems, 178-4-4 Wakashiba, Kashiwa, Chiba 277-0871, Japan

[2] Japan Atomic Energy Agency, Fukushima Environmental Safety Center, 45-169 Sukakeba, Kaibana, Haramachi-ku, Minamisoma City, Fukushima 975-0036, Japan

[3] Japan Atomic Energy Agency, Fukushima Environmental Safety Center, 10-2 Fukasaku, Miharu-machi, Tamura-gun, Fukushima 963-7700, Japan

[4] Research Organization for Information Science and Technology, 2-4 Shirakata, Tokai-mura, Ibaraki-ken 319-1106, Japan

[*]Corresponding author: kim.misik@jaea.go.jp

Highlights

- Simulations of $\dot{H}^*(10)$ at three suburban locations near to FDNPP with 3D models of individual buildings, trees and roads.
- Correlation demonstrated between simulated and measured $\dot{H}^*(10)$.
- $\dot{H}^*(10)$ was on average 5.0% higher when buildings and trees were removed from the models.
- Low retention of ^{134}Cs and ^{137}Cs by buildings and asphalt was on average more important than shielding by buildings.
- The results help clarify the extent to which buildings, trees and asphalt affect $\dot{H}^*(10)$ at these sites.

Abstract

The influence of buildings, trees and paved surfaces on outdoor ambient dose equivalent rates ($\dot{H}^{*}(10)$) in suburban areas near to the Fukushima Dai-ichi Nuclear Power Plant (FDNPP) was investigated with Monte Carlo simulations. Simulation models of three un-decontaminated sites in Okuma and Tomioka were created with representations of individual buildings, trees and roads created using geographic information system (GIS) data. The ^{134}Cs and ^{137}Cs radioactivity distribution within each model was set using in-situ gamma spectroscopy measurements from December 2014 and literature values for the relative radioactive cesium concentration on paved surfaces, unpaved land, building outer surfaces, forest litter and soil layers, and different tree compartments. Reasonable correlation was obtained between the simulations and measurements for $\dot{H}^{*}(10)$ across the sites taken in January 2015. The effect of buildings and trees on $\dot{H}^{*}(10)$ was investigated by performing simulations removing these objects, and their associated ^{134}Cs and ^{137}Cs inventory, from the models. $\dot{H}^{*}(10)$ were on average 5.0% higher in the simulations without buildings and trees, even though the total ^{134}Cs and ^{137}Cs inventory within each model was slightly lower. The simulations without buildings and trees were then modified to include ^{134}Cs and ^{137}Cs in the ground beneath locations where buildings exist in reality, and the inventory of paved surfaces modelled as if they had high retention of ^{134}Cs and ^{137}Cs fallout like soil areas. $\dot{H}^{*}(10)$ increased more markedly in these cases than when considering the shielding effect of buildings and trees alone. These results help clarify the magnitude of the effect of buildings, trees and paved surfaces on $\dot{H}^{*}(10)$ at the un-decontaminated sites within Fukushima Prefecture.

Keywords: ambient dose equivalent rate; modelling; Fukushima accident; Monte Carlo; PHITS

1. Introduction

The ambient dose equivalent rate ($\dot{H}^*(10)$ in μSv/h) at 1 m above the ground is used to quantify radiation levels in areas contaminated with fallout from nuclear power plant accidents (IAEA, 2006; Saito and Petoussi-Henss, 2014; Andoh et al., 2015; Mikami et al., 2015). The relationship between radioactive fallout and $\dot{H}^*(10)$ is complicated as $\dot{H}^*(10)$ strongly depends on the local distribution of fallout radionuclides within the environment, and shielding by terrain, buildings, vegetation, etc. (Jacob and Meckbach, 1987; ICRU, 1994; Furuta and Takahashi, 2015; Malins et al., 2015a, 2016; Gonze et al., 2016; Ishizaki et al., 2017). Radioactivity concentrations can vary significantly even within a single land cover and use. Tyler et al. (1996) and Mishra et al. (2015) reported large variations between the radioactivities of environmental samples collected repeatedly. Systematic variations also exist between the radioactivity of different land uses, as forests, buildings, paved and unpaved surfaces all retain radioactive fallout to different extents under the influence of various environmental and anthropogenic processes (Evrard et al., 2015; Akimoto, 2015).

Yoshimura et al. (2017) recently studied the retention of radioactive cesium within un-decontaminated urban areas four years after the Fukushima Dai-ichi Nuclear Power Plant (FDNPP) accident. They found that ^{134}Cs and ^{137}Cs had largely been removed from paved surfaces, which retained less than 20% of the initial radioactive cesium fallout on average. Inclined and vertical surfaces on the outside of buildings (walls, windows, pitched roofs etc.) retained less than 2% of the initial fallout on average, while the corresponding result for horizontal building surfaces (e.g. flat roofs and gutters) was below 10%.

The inhomogeneous distribution of radioactive cesium in the environment has been used to explain why $\dot{H}^*(10)$ inside buildings are generally lower than outdoors (Matsuda et al., 2017). A review by Yoshida-Ohuchi et al. (2018) found that $\dot{H}^*(10)$ reduction factors for light-construction wooden buildings in Fukushima Prefecture are typically in the range 0.38-0.55, and for heavier construction buildings, such as steel-reinforced concrete buildings, in the range 0.1-0.19. Matsuda et al. (2017) suggested that the magnitude of the reduction factors for light-construction buildings was mainly a consequence of the ‘un-contaminated effect’. Here the patch of un-contaminated ground beneath the building causes $\dot{H}^*(10)$ to be lower indoors, as points indoors have greater separation from the radioactive source than points outdoors. For heavier-construction buildings, Matsuda et al. (2017) proposed that the even smaller reduction factors were a consequence of both the un-contaminated effect and the substantial shielding capacity of the building walls.

The amount of radioactive ^{134}Cs and ^{137}Cs in trees tends to be small a few years after a radioactive fallout event (Gonze and Calmon, 2017). Imamura et al. (2017a) reported measurements from 2014 indicating that only 2-10% of all ^{137}Cs in forests (both conifer and deciduous) was present in the aboveground biomass. The rest of the ^{137}Cs was present in the forest litter layer and the underlying soil.

Previously Jacob and Meckbach (1987) used Monte Carlo simulations to investigate how the varying contamination levels of different environmental surfaces, e.g. lawns, buildings, trees and paved areas, affect air kerma rates in models of typical European urban and suburban areas. Kis et al. (2004) performed a similar Monte Carlo analysis for an industrial area. Eged et al. (2006) reviewed various Monte Carlo models developed for simulating external doses in urbanized areas. More recently there have been developments in creating realistic Monte Carlo models of urban environments by using data from geographic information systems (GIS) (Kramer et al., 2013; Li et al., 2015).

In this study Monte Carlo simulations were used to investigate the effects of buildings, trees and paved surfaces on $\dot{H}^*(10)$ at three un-decontaminated suburban sites near to the FDNPP. The models incorporated representations of individual buildings, trees and roads based on GIS data. The radioactive cesium distribution in the models was assigned based on in-situ measurements of radioactivities from December 2014, and the results validated against $\dot{H}^*(10)$ measurements from January 2015. It was expected that the main effect of buildings and trees would be to shield gamma rays and lower $\dot{H}^*(10)$ compared to open areas of land, as the ^{134}Cs and ^{137}Cs inventories retained by buildings and trees are low. This hypothesis was tested by comparing simulations that included models of buildings and trees to simulations without these features. Further simulations were conducted to investigate the effects of different retention rates of radioactive cesium fallout between surface types. Ground covered by buildings and asphalt in the first simulations was instead modelled as open areas of soil with high radioactive cesium retention. The effects of radioactive cesium loss from building outer surfaces and paved areas on $\dot{H}^*(10)$ were quantified by comparing the different simulation cases.

2. Methods

2.1 Study areas

Two sites in Okuma Town, Fukushima Prefecture, denoted sites A and B, and one site in Tomioka Town, Fukushima Prefecture, denoted site C, were modelled in this study. Sites A and B are located ~5 km west of the FDNPP, and site C is located ~7 km to the south of the FDNPP (Fig. 1(a)). All three sites were evacuated in March 2011 due to receiving large amounts of radioactive fallout from the FDNPP accident, and are classified as zones where it is difficult to allow the return of residents (Ministry of Economy, Trade and Industry, 2017). No decontamination work had taken place prior to December 2014 when the measurement surveys reported in this paper were conducted.

A model was created of a 200×200 m square area of land at each site. Site A consists of abandoned wooden residential houses and rice paddies, along with a Japanese cedar plantation in the north-west quadrant (Fig. 1(b)). Site B, located 200 m to the south of site A, contains two large, single-story, wooden community buildings and a farm (Fig. 1(c)). Site C includes concrete and wood-frame residential buildings, rice paddies and a small Japanese cedar plantation (Fig. 1(d)).

2.2 Model creation

2.2.1 Land topography

The simulation models of sites A, B and C were created using bespoke software developed for creating 3D representations of the land surface topography, buildings and trees at sites in North East Japan. Digital Elevation Model (DEM) data, representing the elevation above sea level (a.s.l.) of the land surface (excluding man-made structures or vegetation), were extracted for each of the sites from larger datasets covering Fukushima Prefecture (Geospatial Information Authority of Japan, 2012; RESTEC, 2017). The horizontal resolution of the DEM data was 0.5-2.0 m. The land surface topography was modelled using a triangular mesh of 10×10 m cells (Fig. 2, pastel green lines). The elevation a.s.l. of each vertex on the mesh was set to the value of the nearest datum in the DEM dataset. Sites A, B and C are located in relatively flat lowland areas of Fukushima Prefecture. The maximum difference in elevation between the highest and lowest vertices on the triangular meshes was 4.2 m for sites A and B, and 3.1 m for site C (Table 1).

2.2.2 Buildings

The locations of individual buildings within each site were determined using ortho-photographs of the areas (Geospatial Information Authority of Japan, 2012; RESTEC, 2017). Rectangular boundary lines were drawn around the footprint area of each building (Fig. 2, blue lines). The width and breadth of each building model was set according to these rectangles.

Individual buildings were modelled following the designs used by Furuta and Takahashi (2015) in Monte Carlo simulations for the dose reduction factors of typical Japanese buildings.

Three classes of building were modelled: wooden construction, concrete construction, and sheet metal buildings. Wooden buildings were predominantly single or two story houses or community buildings. Concrete buildings were either two or three story apartment blocks. Sheet metal buildings were all single story storage buildings or workshops. The number of stories of each building was determined using Google Street View (Google, 2017). Wooden buildings were given either hip or gable roofs, based on the ortho-photographs, while the concrete and sheet metal buildings were all assigned flat roofs.

Building heights, construction materials and densities were the same as those used by Furuta and Takahashi (2015). Full details on the building models are given in Fig. S1 and Table S1. Furuta and Takahashi (2015) found that wooden buildings with 2 cm thick walls gave $\dot{H}^*(10)$ dose reduction factors in the range 0.4-0.6, which is consistent with measurements from Fukushima Prefecture (Yoshida-Ohuchi et al., 2018). Likewise concrete buildings with 15 cm thick walls gave reduction factors in the range 0.1-0.2 (Furuta and Takahashi, 2015), again consistent with the measured range (Yoshida-Ohuchi et al., 2018). Therefore these wall thicknesses were adopted in this study. The numbers of buildings in each type in the completed 3D models of sites A, B and C, along with the total land area occupied by buildings, are listed in Table 1.

2.2.3 Trees

Trees were modelled as either Japanese cedars or konara oaks. Sites A and C contain small Japanese cedar plantations. The area of each plantation (Table 1) was determined by the number of cells of the triangular mesh covered by the plantation, as indicated by the ortho-photographs. Imamura et al. (2017a, 2017b) reported measurements of a plantation of Japanese cedars in Otama, Fukushima Prefecture, including tree density (ha^{-1}), mean height (m), mean diameter at breast height (m), and mean aboveground biomass (kg/m^2). The 3D models of the plantations within sites A and C were based on the Otama plantation data. In total 212 and 95 Japanese cedars were randomly inserted into the plantation areas of sites A and C respectively, in accordance with the tree density reported for the Otama plantation.

Each Japanese cedar tree was modelled as a cylindrical trunk consisting of outer bark and inner wood sections, and an upper cone of diffuse organic material representing the branches and needles (Fig. S2). The dimensions of these components, along with the material densities (Table S2), were all determined based on the mean tree height, diameter at breast height, and biomass of the cedars in the Otama plantation (Imamura et al., 2017a; 2017b; Ohashi et al., 2017).

Other trees spread across sites B and C were modelled as deciduous konara oaks. These trees were added manually into the models in locations where individual trees were identifiable on the ortho-photographs. The modelling parameters for these trees were based on measurements of konara oaks in a plantation in Kawauchi, Fukushima Prefecture, reported by Imamura et al. (2017a) and Ohashi et al. (2017). Each konara oak was modelled as a cylindrical trunk of bark and wood, and an upper ellipsoid of organic material to represent the branches and leaves (Fig. S2). The dimensions and material densities (Table S3) of the konara oak tree models were set in accordance with the measurements of Imamura et al. (2017a) and Ohashi et al. (2017). Total numbers of trees in the completed 3D models are listed in Table 1.

2.2.4 Ground types

The ground within each cell on the 10×10 m triangular mesh was assigned as either asphalt or soil type. Cells were modelled as paved surfaces if the ortho-photograph indicated the main cell coverage was a road or a paved parking lot (Fig. 3, dark grey areas). The ground in paved cells consisted of a dense surface layer representing asphalt, followed by soil beneath (Table S4).

The ground in other cells was modelled as soil. Soil cells were subdivided into three categories depending on the main land cover indicated by the ortho-photograph. Ground in uncovered areas, such as paddy fields, farmland and gardens, was modelled as eight layers of soil (Fig. 3, light green areas) with thicknesses and densities given in Table S5. The ground in the Japanese cedar plantations at sites A and C, was modelled as four layers of soil topped by a layer of forest litter (Fig. 3, green areas). Soil and litter layer thicknesses and densities (Table S6) followed Imamura et al. (2017a). Land underneath buildings was modelled as eight layers of soil (Fig. 3, brown areas), similar to the uncovered areas (Table S5).

The 10×10 m triangular mesh was somewhat coarse for representing the ground surface type in the built-up areas of each site, in particular around buildings where the surface type in reality changes on the meter-scale between building foundations, gardens and paved surfaces. The choice for the 10×10 m mesh size was made as a trade-off against the computational memory requirements of the large PHITS models created by this modelling process.

2.2.5 Inventory and distribution of ^{134}Cs and ^{137}Cs within the models

In situ gamma spectroscopy measurements of the ^{137}Cs inventory retained by three paved surfaces at sites B and C were performed in December 2014 (Table S7). These measurement results, coupled with measurements reported by Yoshimura et al. (2017) for the relative concentration of ^{137}Cs on different environmental surfaces, were used to assign the ^{137}Cs distribution within the simulation models.

The ^{137}Cs inventory of paved surfaces at sites A and B used in the models (Table S8) was derived from the mean of the two inventory measurements at site B, followed by decay-correction to the applicable simulation date (January 18, 2015). The ^{137}Cs inventory of paved surfaces at site C was derived from the paved ground measurement at site C. The ^{137}Cs inventory of the paved areas was modelled as being dispersed homogeneously within the top

0.1 cm layer of the ground (Table S4), as radioactive cesium only penetrates small distances into asphalt surfaces (ICRU, 1994; Inoue et al., 2017).

The total inventory of unpaved areas, such as paddy fields, gardens, farmland and forests, was set in proportion to the inventory of paved surfaces. Yoshimura et al. (2017) reported a ratio of 0.18 for the inventory of paved surfaces relative to the initial fallout on neighboring unpaved permeable surfaces. The ^{137}Cs inventories of unpaved surfaces and forests in the simulation models were determined using this factor and appropriate decay correction to the simulation modelling date (Table S8).

In uncovered areas (paddy fields, gardens etc.) the ^{137}Cs inventory was apportioned between the eight soil layers approximating an exponential depth distribution with a relaxation mass depth of 2.86 g/cm^2 (Table S5). This relaxation mass depth is a representative value for unpaved and open sites on January 18, 2015 according to equation (1) of Yoshimura et al. (2017). For the Japanese cedar forests at site A and C, the total ^{137}Cs inventory listed in Table S8 was apportioned between the tree compartments, forest litter, and forest soil layers according to the Imamura et al. (2017a) measurements of the Japanese cedar plantation in Otama (Tables S2 and S6). The inventory of konara oak trees (Table S3) followed the measurements made in fall 2014 for the Kawauchi plantation (Imamura et al., 2017a).

The ^{137}Cs inventory on the outer surfaces of buildings, i.e. walls, windows and roofs, (Table S8) was calculated based on a factor 0.012 for the relative inventory for the building surfaces compared to the initial fallout on unpaved ground (Yoshimura et al., 2017). All ^{134}Cs inventories in the model were assigned in proportion to the corresponding ^{137}Cs inventory. The ^{134}Cs/^{137}Cs activity ratio used was 0.30, which is the value applicable on January 18, 2015 assuming a ^{134}Cs/^{137}Cs activity ratio of 1.0 on March 11, 2011.

2.3 Monte Carlo simulations

The distribution of $\dot{H}^*(10)$ at 1 m above the ground within the models was simulated using the Particle and Heavy Ion Transport code System (PHITS). PHITS is Monte Carlo radiation transport code developed by a collaboration of research institutions in Japan and Europe (PHITS, 2017; Sato et al., 2018). The 3D models of sites A, B and C were exported from the model creation software and converted into PHITS input files. The various features in the 3D models (land topography, ground layers, building structures, trees etc.) were represented by PHITS surface, cell and coordinate transform functions. Cesium-134 and ^{137}Cs radioactive sources were defined using cylindrical, rectangular and triangular prism source types. Gamma ray emission intensities were calculated for each source region in the models based on the ^{134}Cs and ^{137}Cs radioactivity concentrations in Tables S2 to S6 and S8.

To evaluate the effects of shielding and the distribution of ^{134}Cs and ^{137}Cs in the environment on $\dot{H}^*(10)$, three simulations of each site were performed with the inclusion of different features of the models (Table 2). The first simulations (case 1, Figs. 3 and 4(a)) included all buildings and trees in the model, and ^{134}Cs and ^{137}Cs were present on building external surfaces, within tree canopies, bark and wood.

In the second simulations (case 2, Fig. 4(b)) the buildings and trees, and their associated ^{134}Cs and ^{137}Cs radioactivity, were removed from the model. The purpose of the case 2 simulations was to evaluate the shielding effect of buildings and trees on $\dot{H}^*(10)$ within each area.

The third simulations (case 3, Fig. 4(c)) were similar to the case 2 simulations in that the buildings and trees were removed from the models. The additional difference was ^{134}Cs and ^{137}Cs was added into the ground in cells occupied by buildings in the case 1 simulations. The radioactivity and depth distribution of these cells was set equal to the values for the uncovered soil areas at the same site (Table S5). The purpose of the case 3 simulations was to evaluate the extent that radioactive cesium loss from building outer surfaces due to weathering, and the lack of contamination of soil beneath buildings, has on lowering outdoor $\dot{H}^*(10)$ values.

The PHITS simulations were executed on a seven node computing cluster with dual Intel Xeon 2.67 GHz 12-core processors. $\dot{H}^*(10)$ at 1 m above the surface was tallied on a mesh with 10×10 m cells covering each study site. Each simulation consisted of 332 million gamma ray histories, which was sufficient to converge the relative errors of all tallies to below 3%. A 0.05 μSv/h contribution was added to the result of each tally to represent the contribution of the terrestrial gamma-ray component of natural background radiation to $\dot{H}^*(10)$ values in the environment (Mikami et al., 2015; Yasutaka et al., 2013).

Only tally regions within the central 160×160 m part of the 200×200 m study areas were used for the analysis. The underestimation of $\dot{H}^*(10)$ in simulation tallies at the edge of the central 160×160 m area by failure to simulate ^{134}Cs and ^{137}Cs present outside the full 200×200 m model would be lower than 15% assuming a spatially homogeneous ^{134}Cs and ^{137}Cs distribution (Malins et al., 2015b; Malins et al., 2016). As the focus of this study was $\dot{H}^*(10)$ in the outdoor environment, 10×10 m tally regions which overlapped by more than 50% by area with the inside of buildings were excluded from the analysis. The entire modelling process is summarized with a schematic in Fig. S3.

2.4 Comparison with measurements of $\dot{H}^*(10)$

Simulated $\dot{H}^*(10)$ were compared against $\dot{H}^*(10)$ measurements taken on December 10, 2014 using KURAMA-II apparatus. KURAMA-II consists of a CsI scintillator, GPS device and CompactRIO controller by National Instruments (Tsuda et al., 2014; Tanigaki et al., 2015). The KURAMA-II apparatus was carried in a backpack by an operator on foot through the three sites. To offset operator related attenuation effects (Buchanan et al., 2016), the KURAMA-II measurements were corrected to estimate $\dot{H}^*(10)$ at 1 m above the surface in the absence of the operator and detection equipment. No decay correction was applied to the measurement results for comparison with the simulation results, which apply on January 18, 2015. The measurements were compared to the simulation results by taking the average of all measurement points coincident with each 10×10 m simulation tally region.

3. Results and discussion

3.1 Comparison between simulation and measurement results

$\dot{H}^*(10)$ at 1 m above the ground from the case 1 simulations (including buildings and trees) and the KURAMA-II measurements are shown in Fig. 5. The simulated $\dot{H}^*(10)$ in built-up areas are generally lower than for areas with open agricultural land and Japanese cedar plantations (Fig. 6). This result is expected as the ^{134}Cs and ^{137}Cs inventories on buildings and asphalt surfaces are lower than the inventories of unpaved agricultural land and forest areas, and because shielding by buildings and trees acts to lower $\dot{H}^*(10)$.

Fig. 6 shows the correlation between the case 1 simulation results and the averaged measurements in each 10×10 m tally region. The majority of the simulation results are within a factor 2 of the measurement results. The root mean square deviation (RMSD) of the simulation results from the measurements is 1.6 μSv/h, when considering sites A, B and C collectively (Table 3).

The mean absolute percentage deviation (MAPD) between the simulations and measurements is 23% over all sites. This result is comparable with the MAPD of 30% found by Malins et al. (2016) in more simplistic simulation models for $\dot{H}^*(10)$ above flat, undisturbed fields (locations away from buildings and trees) across Fukushima Prefecture. In that study the main source of error in the simulation results was attributed to uncertainty in the input ^{134}Cs and ^{137}Cs radioactivity values. There is similar uncertainty in the simulations in this study. The inputted ^{134}Cs and ^{137}Cs radioactivities are all derived from in situ gamma spectroscopy measurements of the inventory of paved surfaces at sites B and C (Table S7). Therefore the simulations cannot account for fluctuations of ^{134}Cs and ^{137}Cs levels across each site, which are typical in fallout contaminated areas (Tyler et al., 1996). This limitation is expected to be the main factor underlying the scatter of the data points in Fig. 6.

The Pearson correlation coefficients for sites A (0.62) and B (0.54) are higher than for site C (0.26). The largest Pearson correlation coefficient is for all sites collectively (0.77). This suggests the range of measured $\dot{H}^*(10)$ across the sites (Table 3), and hence the range of ^{137}Cs inventories, is a factor affecting the Pearson correlation coefficients.”

3.2 Effect of ^{134}Cs and ^{137}Cs inventory on buildings and trees on $\dot{H}^*(10)$

It was expected that the contribution to $\dot{H}^*(10)$ of the ^{134}Cs and ^{137}Cs inventory adhering to the outer surfaces of buildings, and the inventory within trees, would be minor. This is because this ^{134}Cs and ^{137}Cs inventory totals less than 1% of the entire ^{134}Cs and ^{137}Cs inventory at each site (Table 2). A variation of the case 1 simulation for site A was performed to check this hypothesis. This simulation included the building and tree models but set their associated ^{134}Cs and ^{137}Cs radioactivities to zero. $\dot{H}^*(10)$ from this simulation were on average 0.8% lower than from the results of the original case 1 simulation, which included the ^{134}Cs and ^{137}Cs inventory associated with buildings and trees, thus confirming the hypothesis.

3.3 Effect of shielding by buildings and trees on $\dot{H}^*(10)$

The case 1 simulations were modified into the case 2 simulations by removing the buildings and trees from the models (Fig. 4(b)). On average over all sites, $\dot{H}^*(10)$ was 5.0% higher in the case 2 simulations than the case 1 simulations (Table 4). The low importance of the ^{134}Cs and ^{137}Cs inventory on buildings and trees means that the shielding they provide must be the main explanation for this difference in results between the case 1 and case 2 simulations.

3.4 Effect of ^{134}Cs and ^{137}Cs loss from buildings on $\dot{H}^{*}(10)$

The effect on $\dot{H}^{*}(10)$ of the lower retention of ^{134}Cs and ^{137}Cs by buildings than soil areas was investigated by performing the case 3 simulations. The case 3 simulations were variations of the case 2 simulations, i.e. without building and tree models, that were modified to include ^{134}Cs and ^{137}Cs within the ground in 'building' cells on the triangular mesh (cf. Fig. 4 (b) and (c)). The radioactivities and depth distribution used were the same as for the unpaved open areas (Table S5).

$\dot{H}^{*}(10)$ from the case 3 simulations were on average 15% higher than from the case 1 simulations, which included the buildings and trees (Table 4). The case 3 simulation results were 10% higher than the comparable case 2 simulation results on average. This difference suggests that on average the low retention of ^{134}Cs and ^{137}Cs by building outer surfaces and the lack of contamination beneath buildings is of greater importance than shielding by buildings and trees for $\dot{H}^{*}(10)$ over these three sites. It is not possible to generalize this result to specific locations within the sites however. The relative importance of these two factors at any specific location depends on the size of the buildings and trees, as well as the types, thicknesses and densities of their materials.

3.5 Effect of ^{134}Cs and ^{137}Cs loss from paved surfaces on $\dot{H}^{*}(10)$

$\dot{H}^{*}(10)$ above roads and paved parking areas in Fukushima Prefecture are generally lower than $\dot{H}^{*}(10)$ above neighboring unpaved land (Takeishi et al., 2017). In a similar manner to the outer surfaces of buildings, ^{134}Cs and ^{137}Cs fallout is easily cleaned off from asphalt surfaces by natural weathering processes (ICRU, 1994). A calculation was performed to quantify the effect of ^{134}Cs and ^{137}Cs loss from paved surfaces on $\dot{H}^{*}(10)$. In the calculation, each site was modelled as an infinite half-space geometry (ICRU, 1994), representing a wide and open area of ^{134}Cs and ^{137}Cs contaminated soil, without features such as land topography, building and trees. The ^{134}Cs and ^{137}Cs inventory was dispersed in soil as per the unpaved and open areas in simulation cases 1-3 (Table S5). $\dot{H}^*(10)$ were estimated using conversion coefficients for radioactivity distributed exponentially within soil (Saito and Petoussi-Henss, 2014; Malins et al., 2016). The results of these calculations are equivalent to modifying the case 3 simulations to model asphalt areas as soil areas instead. Note land topography is not a significant factor affecting $\dot{H}^*(10)$ at these three sites due to their flat nature.

$\dot{H}^*(10)$ from the open field calculations were significantly higher than those from the case 1 simulations, by 48% on average (Table 4). This represents an additional 33% increase in average $\dot{H}^*(10)$ over the case 3 simulations. The total area of paved land at sites A, B and C is greater than the area occupied by buildings (Table 1). Thus the result suggests the loss of ^{134}Cs and ^{137}Cs fallout from asphalt surfaces is more important for $\dot{H}^*(10)$ across these three sites than the loss from building out surfaces. This is despite the fact that the radioactive cesium retention ratio of paved surfaces was measured as being slightly higher than that of building outer surfaces (Yoshimura et al., 2017).

Collectively the results in Table 4 highlight the significance of ^{134}Cs and ^{137}Cs loss from the outer surfaces of buildings and from paved surfaces in reducing $\dot{H}^*(10)$ within suburban areas compared to locations that have not been built up. An important aspect that needs to be considered is the ultimate fate of this ^{134}Cs and ^{137}Cs. A component of the washed-off ^{134}Cs and ^{137}Cs ends up in storm drains, and ultimately transfers through surface water management systems and through rivers (Pratama et al., 2014, 2015). Some radioactive cesium also accumulates along the borders and verges of paved areas and around the edges of buildings (Akimoto, 2015). This ^{134}Cs and ^{137}Cs will contribute to $\dot{H}^*(10)$ in reality, but was not modelled explicitly in the simulations described above.

4. Conclusions

Models were developed of three suburban sites near to FDNPP for Monte Carlo simulations of $\dot{H}^*(10)$. The topography, structures, trees and land use at each site were modelled using DEM data and ortho-photographs. The distribution of ^{134}Cs and ^{137}Cs within the models was set based on in situ measurements of the radioactivity of different land uses and urban surfaces from December 2014, and literature values for the partitioning of ^{134}Cs and ^{137}Cs radioactivity in Fukushima forests.

The results from the full-detail simulations, i.e. including models of individual buildings and trees (case 1), showed reasonable correlation with KURAMA-II measurements taken at each site in January 2015. The quality of the agreement between the simulations and the measurements at these suburban sites was comparable to the results found by Malins et al. (2016) for simulations of open field sites. It was assumed that the main factor limiting the accuracy of the simulation predictions for $\dot{H}^*(10)$ was the uncertainty in the input ^{134}Cs and ^{137}Cs distributions to the models. However only a limited number of inventory measurements were available for the study sites, so it was not possible to quantify the uncertainties in the input activity distributions.

Different simulation cases were compared to evaluate the effects of shielding by buildings and trees, and the low retention of ^{134}Cs and ^{137}Cs by building outer surfaces and paved areas, on $\dot{H}^*(10)$. On average, the losses of ^{134}Cs and ^{137}Cs from building outer surfaces and paved areas were more important for lowering $\dot{H}^*(10)$ across the three sites than shielding by buildings and trees. However this result cannot be generalized to specific locations, as the relative importance of these factors depends locally on the sizes of the buildings, trees and asphalt areas, as well as the material types, thicknesses and densities at each location.

We encourage future studies to measure the relative radioactivity levels of areas known to accumulate radioactive cesium due to wash off and weathering processes, such as areas around the edges of buildings, roads and paved parking areas. This information would be useful to use in simulations to quantify the importance of these accumulations for $\dot{H}^*(10)$. Other potential applications of the modelling approach described in this study include understanding the temporal dynamics of $\dot{H}^*(10)$ within fallout contaminated areas in Fukushima Prefecture, and studies evaluating remediation options for as yet un-decontaminated sites.

Acknowledgements

We wish to thank the towns of Okuma and Tomioka for their permission to study these test sites and the Geospatial Information Authority of Japan for providing land topography data obtained from an aerial laser survey. We thank NTT DATA and RESTEC for providing the AW3D ortho-photograph of site A. We also thank Dr. Kimiaki Saito, Dr. Kazuki Iijima and colleagues in JAEA’s Center for Computational Science & e-Systems and Fukushima Environmental Safety Center for their support and encouragement towards this research.

References

Akimoto, K., 2015. Extreme variations of air dose rates in east Fukushima. Radiat. Prot. Dosim. 167, 336-339. DOI:10.1093/rpd/ncv274

Andoh, M., Nakahara, Y., Tsuda, S., Yoshida, T., Matsuda, N., Takahashi, F., Mikami, S., Kinouchi, N., Sato, T., Tanigaki, M., Takamiya, K., Sato, N., Okumura, R., Uchihori, Y., Saito, K., 2015. Measurement of air dose rates over a wide area around the Fukushima Dai-ichi Nuclear Power Plant through a series of car-borne surveys. J. Environ. Radioact. 139, 266-280. DOI:10.1016/j.jenvrad.2014.05.014

Buchanan, E., Cresswell, A.J., Seitz, B., Sanderson, D.C.W., 2016. Operator related attenuation effects in radiometric surveys. Radiat. Meas. 86, 24-31. DOI:10.1016/j.radmeas.2015.12.029

Eged, K., Kis, Z., Voigt, G., 2006. Review of dynamical models for external dose calculations based on Monte Carlo simulations in urbanised areas. J. Environ. Radioact. 85, 330-343. DOI:10.1016/j.jenvrad.2004.04.015

Evrard, O., Laceby, J.P., Lepage, H., Onda, Y., Cerdan, O., Ayrault, S., 2015. Radiocesium transfer from hillslopes to the Pacific Ocean after the Fukushima nuclear power plant accident: a review. J. Environ. Radioact. 148, 92-110. DOI:10.1016/j.jenvrad.2015.06.018

Furuta, T., Takahashi, F., 2015. Study of radiation dose reduction of buildings of different sizes and materials. J. Nucl. Sci. Technol. 52, 897-904. DOI:10.1080/00223131.2014.990939

Geospatial Information Authority of Japan, 2012. DEM data obtained by aerial laser survey. http://www.gsi.go.jp/chubu/minichishiki12.html (In Japanese) (accessed: 06.12.2018)

Gonze, M.A., Mourlon, C., Calmon, P., Manach, E., Debayle, C., Baccou, J., 2016. Modelling the dynamics of ambient dose rates induced by radiocaesium in the Fukushima terrestrial environment. J. Environ. Radioact. 161, 22-34. DOI:10.1016/j.jenvrad.2015.06.003

Gonze, M.A., Calmon, P., 2017. Meta-analysis of radiocesium contamination data in Japanese forest trees over the period 2011–2013. Sci. Total Environ. 601-602, 301-316. DOI:10.1016/j.jenvrad.2017.11.021

Google, 2017. Street View function of Google Maps. URL:https://www.google.co.jp/maps/ (accessed: 11.14.17)

IAEA, 2006. Environmental consequences of the Chernobyl accident and their remediation: 20 years of experience. STI/PUB/1239

ICRU, 1994. Gamma-ray spectrometry in the environment. ICRU Report 53.

Imamura, N., Komatsu, M., Ohashi, S., Hashimoto, S., Kajimoto, T., Kaneko S., Takano, T., 2017a. Temporal changes in the radiocesium distribution in forests over the five years after the Fukushima Daiichi Nuclear Power Plant accident. Sci. Rep. 7, 8179. DOI:10.1038/s41598-017-08261-x

Imamura, N., Akama, A., Ohtani, Y., Kobayashi, M., Tsuboyama, Y., Takahasi, M., 2017b. An estimation of air dose rate from considering of radiocesium distribution in Japanese forests. J. Jpn. For. Soc. 99, 1-9. (In Japanese) DOI:10.4005/jjfs.99.1

Inoue, K., Arai, M., Fujisawa, M., Saito, K., Fukushi, M., 2017. Detailed Distribution Map of Absorbed Dose Rate in Air in Tokatsu Area of Chiba Prefecture, Japan, Constructed by Car-Borne Survey 4 Years after the Fukushima Daiichi Nuclear Power Plant Accident. PLoS ONE 12, e0171100. DOI:10.1371/journal.pone.0171100

Ishizaki, A., Sanada, Y., Ishida, M., Munakata, M., 2017. Application of topographical source model for air dose rates conversions in aerial radiation monitoring. J. Environ. Radioact. 180, 82-89. DOI:10.1016/j.jenvrad.2017.09.028

Jacob, P., Meckbach, R., 1987. Shielding Factors and External Dose Evaluation. Rad. Prot. Dosim. 21, 79-85. DOI:10.1093/oxfordjournals.rpd.a080057

Kis Z., Eged, K., Voigt, G., Meckbach, R., Muller, H., 2004. Modeling of an industrial environment: external dose calculations based on Monte Carlo simulations of photon transport. Health Phys. 86, 161-173.

Kramer, K., Li, A., Madrigal, J., Sanchez, B., Millage, K., 2013. Monte Carlo Modeling of the Initial Radiation Emitted by a Nuclear Device in the National Capital Region. DTRA-TR-13-045. http://www.dtic.mil/docs/citations/ADA588161 (accessed 09.22.17)

Li, A., Lekoudis, G., Mosher, S., Evans, T., Johnson, S., 2015. Dose Estimation for Complex Urban Environments Using RUGUD, SWORD, ADVANTG and Denovo. Proceedings of M&C + SNA + MC 2015.

Malins, A., Okumura, M., Machida, M., Saito, K., 2015a. Topographic Effects on Ambient Dose Equivalent Rates from Radiocesium Fallout. In Proceedings of M&C + SNA + MC 2015. arXiv:1502.03892v3

Malins, A., Okumura, M., Machida, M., Takemiya, H., Saito, K., 2015b. Fields of View for Environmental Radioactivity. In Proceedings of the International Symposium on Radiological Issues for Fukushima's Revitalized Future. arXiv:1509.09125v2

Malins, A., Kurikami, H., Nakama, S., Saito, T., Okumura, M., Machida, M., 2016. Evaluation of ambient dose equivalent rates influenced by vertical and horizontal distribution of radioactive cesium in soil in Fukushima Prefecture. J. Environ. Radioact. 151, 38-49. DOI:10.1016/j.jenvrad.2015.09.014

Matsuda, N., Mikami, S., Sato, T., Saito, K., 2017. Measurements of air dose rates in and around houses in the Fukushima Prefecture in Japan after the Fukushima accident. J. Environ. Radioact. 166, 427-435. DOI:10.1016/j.jenvrad.2016.03.012

Mikami, S., Maeyama, T., Hoshide, Y., Sakamoto, R., Sato, S., Okuda, N., Sato, T., Takemiya, H., Saito, K., 2015. The air dose rate around the Fukushima Dai-ichi Nuclear Power Plant: its spatial characteristics and temporal changes until December 2012. J. Environ. Radioact. 139, 250-259. DOI:10.1016/j.jenvrad.2014.08.020

Ministry of Economy Trade and Industry, 2017. http://www.meti.go.jp/english/earthquake/nuclear/roadmap/pdf/gainenzu_201704e.pdf (accessed: 04.09.18)

Mishra, S., Sahoo, S.K., Arae, H., Sorimachi, A., Hosoda, M., Tokonami, S., Ishikawa, T., 2015. Variability of radiocaesium inventory in Fukushima soil cores from one site measured at different times. Radiat. Prot. Dosim. 167, 344-347. DOI:10.1093/rpd/ncv276

Ohashi, S., Kuroda, K., Takano, T., Suzuki, Y., Fujiwara, T., Abe, H., Kagawa, A., Sugiyama, M., Kubojima, Y., Zhang, C., Yamamoto K., 2017. Temporal trends in ^{137}Cs concentrations in the bark, sapwood, heartwood, and whole wood of four tree species in Japanese forests from 2011 to 2016. J. Environ. Radioact. 178-179, 335-342. DOI:10.1016/j.jenvrad.2017.09.008

PHITS, 2017. Particle and Heavy Ion Transport code System. https://phits.jaea.go.jp (accessed: 10.20.17)

Pratama, M.A., Yoneda, M., Yamashiki, Y., Shimada, Y., Matsui, Y., 2014. Modeling Migration of Cs-137 in Sewer System of Fukushima City Using Model for Radionuclide Migration in Urban Environment and Drainage System (MUD). Int. J. Eng. Technol. 6, 402-408. DOI:10.7763/IJET.2014.V6.732

Pratama, M.A., Yoneda, M., Shimada, Y., Matsui, Y., Yamashiki, Y., 2015. Future projection of radiocesium flux to the ocean from the largest river impacted by Fukushima Daiichi Nuclear Power Plant. Sci. Rep. 5, 8408. DOI:10.1038/srep08408

RESTEC, 2017. Remote Sensing Technology Center of Japan: Ortho and Topographic Data. https://www.restec.or.jp/en/ (accessed: 11.14.17)

Saito, K., Petoussi-Henss, N., 2014. Ambient dose equivalent conversion coefficients for radionuclides exponentially distributed in the ground. J. Nucl. Sci. Technol. 51, 1274-1287. DOI:10.1080/00223131

Sato, T., Iwamoto, Y., Hashimoto, S., Ogawa, T., Furuta, T., Abe, S., Kai, T., Tsai, P., Matsuda, N., Iwase, H., Shigyo, N., Sihver, L., Niita, K., 2018. Features of Particle and Heavy Ion Transport code System (PHITS) version 3.02. J. Nucl. Sci. Technol. *online ahead of print*. DOI:10.1080/00223131.2017.1419890

Takeishi, M., Shibamichi, M., Malins, A., Kurikami, H., Murakami, M., Saegusa, J., Yoneya, M., 2017. Using two detectors concurrently to monitor ambient dose equivalent rates in vehicle surveys of radiocesium contaminated land. J. Environ. Radioact. 177, 1-12. DOI:10.1016/j.jenvrad.2017.05.010

Tanigaki, M., Okumura, R., Takamiya, K., Sato, N., Yoshino, H., Yoshinaga, H., Kobayashi, Y., Uehara, A., Yamana, H., 2015. Development of KURAMA-II and its operation in

Fukushima. Nucl. Instrum. Methods Phys. Rev. A 781, 57-64. DOI:10.1016/j.nima.2015.01.086

Tsuda, S., Yoshida, T., Tsutsumi, M., Saito, K., 2014. Characteristics and verification of a car-borne survey system for dose rates in air: KURAMA-II. J. Environ. Radioact. 139, 260-265. DOI:10.1016/j.jenvrad.2014.02.028

Tyler, A.N., Sanderson, D.C.W., Scott, E.M., Allyson, J.D., 1996. Accounting for spatial variability and fields of view in environmental gamma ray spectrometry. J. Environ. Radioact. 33, 213-235. DOI:10.1016/0265-931X(95)00097-T

Yasutaka,T., Naito W., Nakanishi J., 2013. Cost and Effectiveness of Decontamination Strategies in Radiation Contaminated Areas in Fukushima in Regard to External Radiation Dose. PLoS ONE. 8(9), e75308. DOI:10.1371/journal.pone.0075308

Yoshida-Ohuchi, H., Matsuda, N., Saito, K., 2018. Review of reduction factors by buildings for gamma radiation from radiocaesium deposited on the ground due to fallout. J. Environ. Radioact. 187, 32-39. DOI:10.1016/j.jenvrad.2018.02.006

Yoshimura, K., Saito, K., Fujiwara, K., 2017. Distribution of ^{137}Cs on components in urban area four years after the Fukushima Dai-ichi Nuclear Power Plant accident. J. Environ. Radioact. 178-179, 48-54. DOI:10.1016/j.jenvrad.2017.07.021

Figure Captions

Figure 1. (a) Overview showing the locations of the sites modelled within Fukushima Prefecture, and proximity to the Fukushima Dai-ichi Nuclear Power Plant. (b), (c) and (d) Satellite photographs showing the 200×200 m square areas of land modelled at sites A, B and C, respectively. Imagery ©2018 Google. Map data ©2018 ZENRIN.

Figure 2. Screenshots from the bespoke software during the creation process of 3D models of (a) site A, (b) site B and (c) site C. Buildings are shown with blue outlines. Individual Japanese cedar and konara oak trees are shown in light blue and red, respectively. The triangular mesh of the land topography model is shown by thin pastel green lines.

Figure 3. Rendering by PHITS of the completed case 1 simulation models of (a) site A and (b) site B.

Figure 4. Renderings of the three simulation cases for site C. (a) Case 1 (with buildings and trees), (b) case 2 (without buildings and trees), and (c) case 3 (without buildings a trees, and including ^{134}Cs and ^{137}Cs in the cells beneath building locations). Colors are as per legend of Fig. 3.

Figure 5. Distribution of $\dot{H}^*(10)$ at 1 m above surface obtained the from the case 1 simulations (square mesh) and the KURAMA-II measurements (circle markers). Results for 10×10 m tally regions with more than 50% overlap by area with building structures are excluded from the analysis. Satellite imagery ©2018 Google.

Figure 6. Scatter plot showing correlation between case 1 simulation results and $\dot{H}^*(10)$ measurements. Marker shape is used to distinguish each site. Marker color indicates predominant land use in the environ of each 10×10 m region. Dashed lines indicate equality and a factor of two deviation from equality.

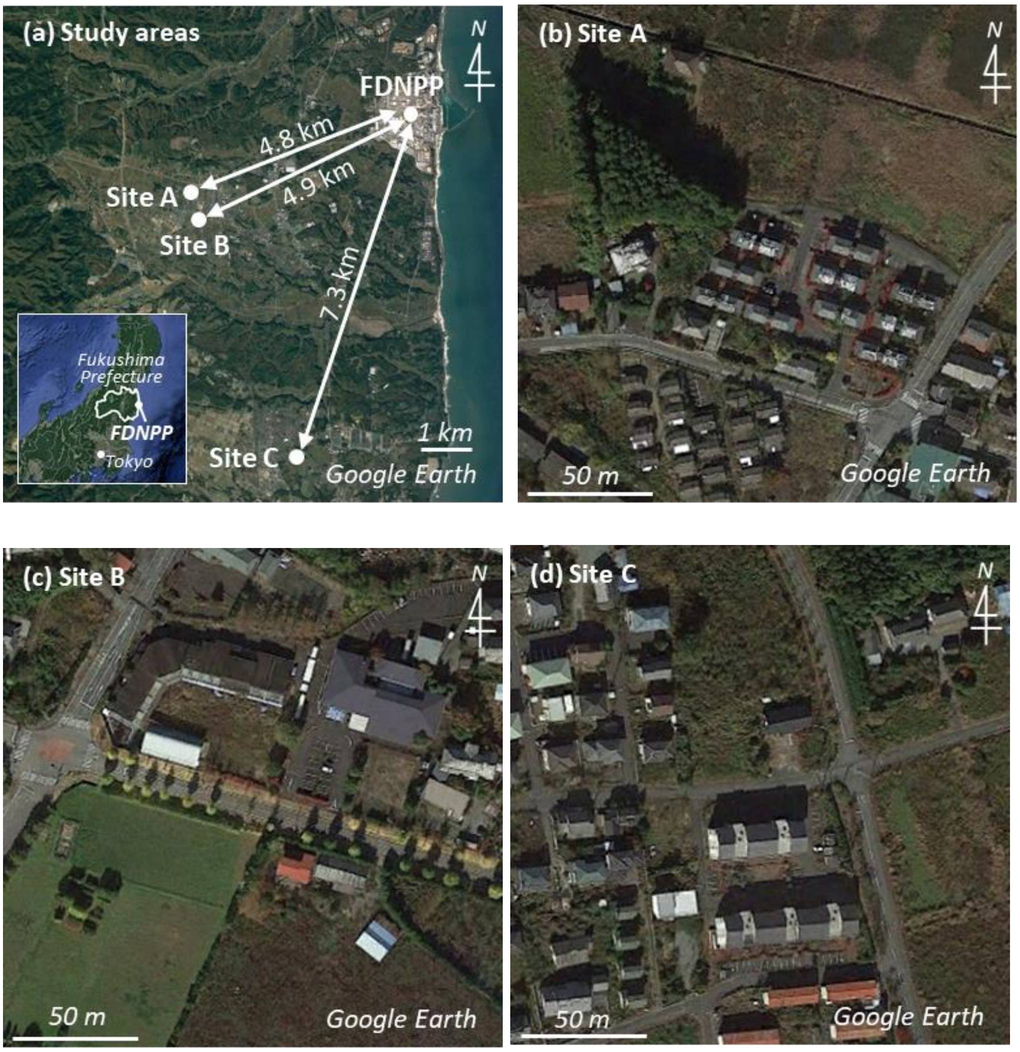
(a) Study areas
N
FDNPP
4.8 km
4.9 km
Site A
Site B
7.3 km
Fukushima
Prefecture
FDNPP
Tokyo
Site C
1 km
Google Earth
(b) Site A
N
50 m
Google Earth
(c) Site B
N
50 m
Google Earth
(d) Site C
N
50 m
Google Earth

Fig. 1

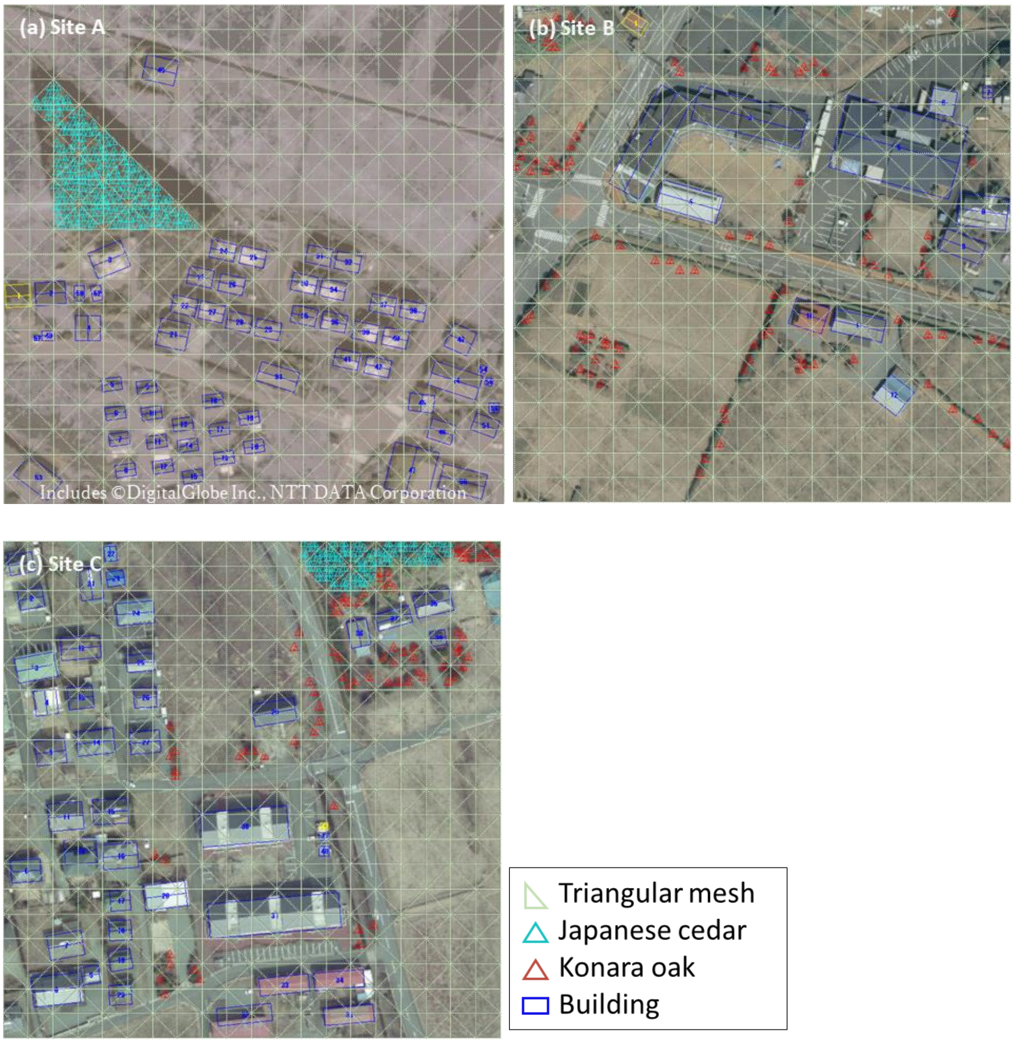
(a) Site A
Includes ©DigitalGlobe Inc., NTT DATA Corporation
(b) Site B
(c) Site C
Triangular mesh
Japanese cedar
Konara oak
Building

Fig. 2

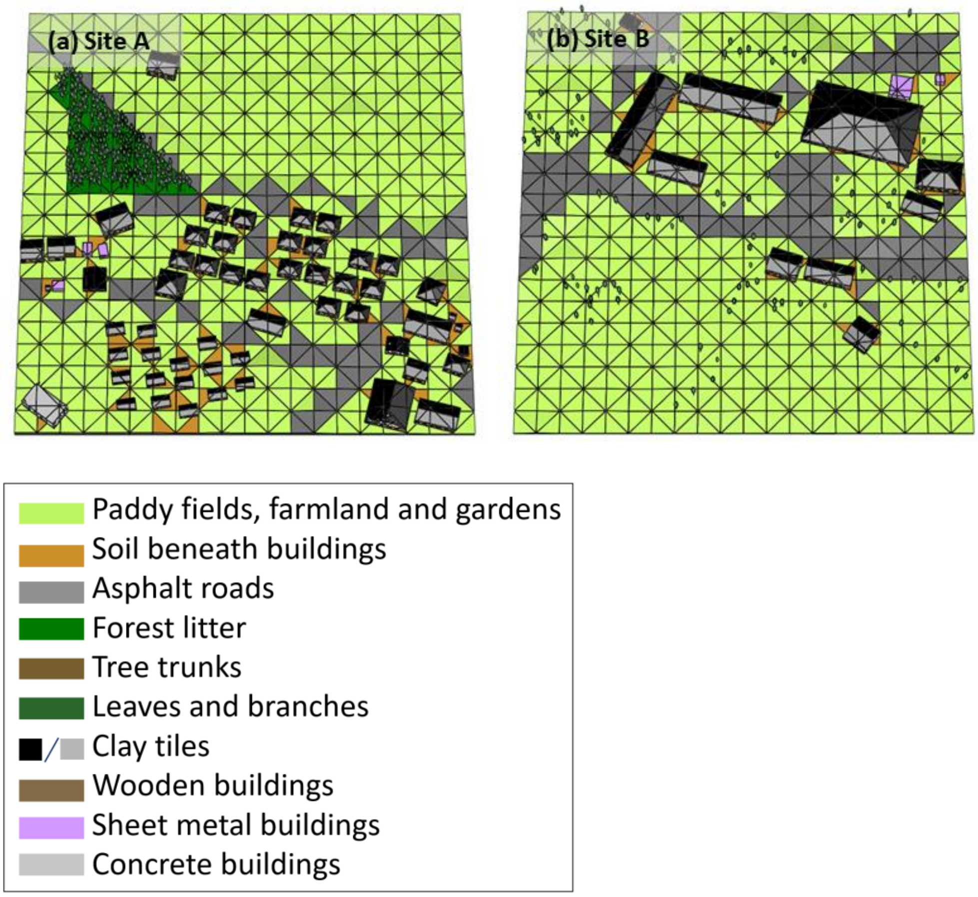
(a) Site A
(b) Site B
Paddy fields, farmland and gardens
Soil beneath buildings
Asphalt roads
Forest litter
Tree trunks
Leaves and branches
Clay tiles
Wooden buildings
Sheet metal buildings
Concrete buildings

Fig. 3

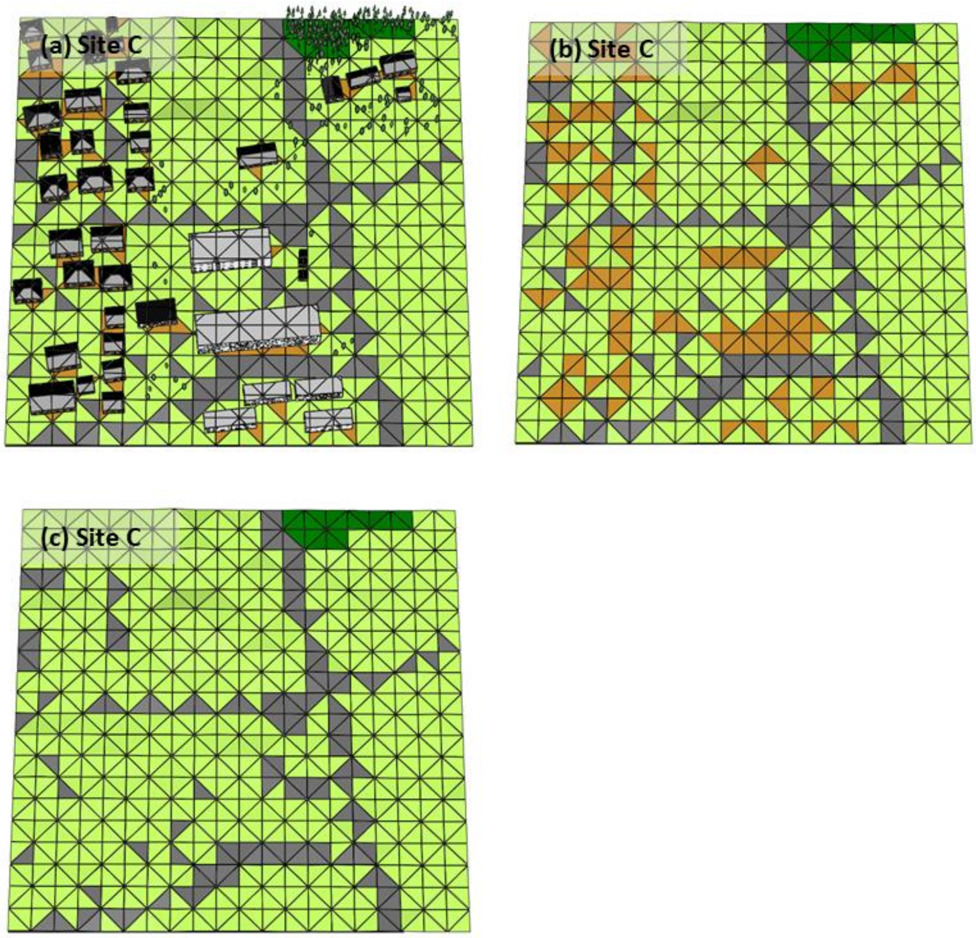

Fig. 4

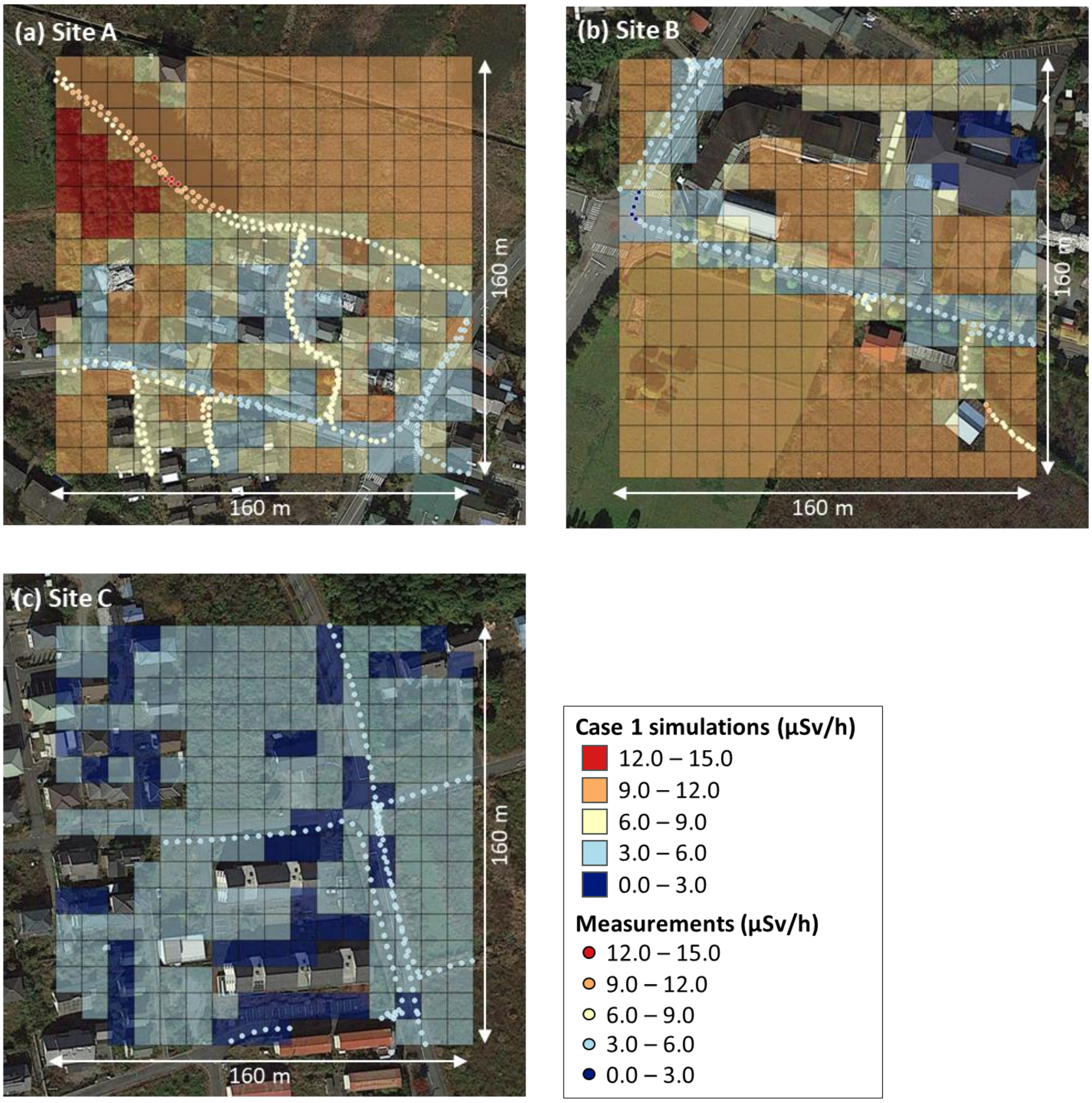
(a) Site A
160 m
160 m
(b) Site B
160 m
160 m
(c) Site C
160 m
160 m
Case 1 simulations (μSv/h)
12.0 – 15.0
9.0 – 12.0
6.0 – 9.0
3.0 – 6.0
0.0 – 3.0
Measurements (μSv/h)
12.0 – 15.0
9.0 – 12.0
6.0 – 9.0
3.0 – 6.0
0.0 – 3.0

Fig. 5

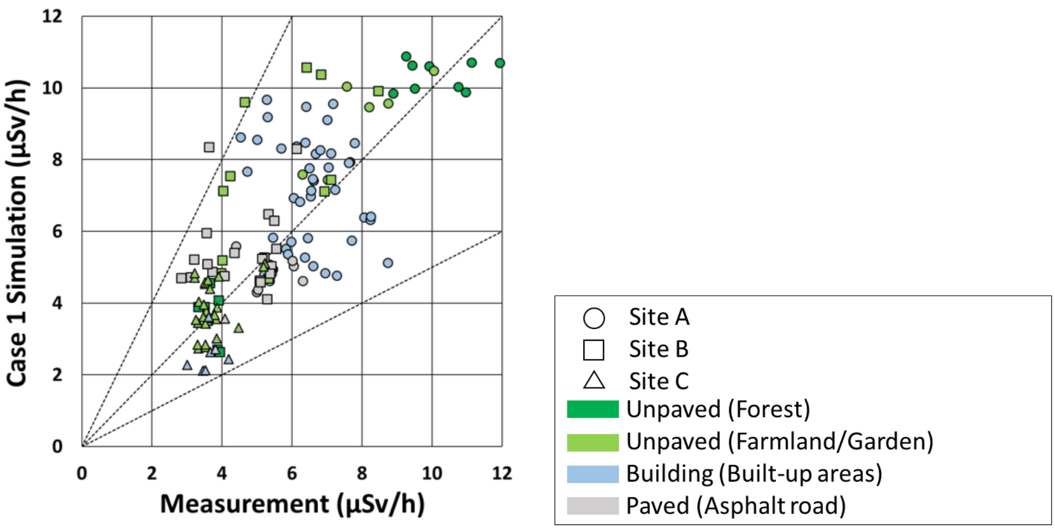
Case 1 Simulation (μSv/h)
Measurement (μSv/h)
0
2
4
6
8
10
12
Site A
Site B
Site C
Unpaved (Forest)
Unpaved (Farmland/Garden)
Building (Built-up areas)
Paved (Asphalt road)

Fig. 6

Table 1. Number of buildings and trees, and other features of models for site A, B and C.

		Site		
		A	B	C
Land surface model	Average elevation a.s.l. (m)	66.1	64.3	51.1
	Minimum elevation a.s.l. (m)	63.9	62.6	49.7
	Maximum elevation a.s.l. (m)	68.1	66.8	52.8
	Area of roads and paved parking lots (m^2)	4150	6400	5700
Buildings	Total footprint area of buildings (m^2)	3700	4000	5100
	Number wooden, single-story	25	7	10
	Number wooden, two-story	29	3	26
	Number concrete, two-story	1	-	4
	Number concrete, three story	-	-	2
	Number sheet metal, single-story	3	2	-
	Total	**58**	**12**	**42**
Trees	Area of Japanese cedar forest (m^2)	1900	**-**	850
	Number Japanese cedars	212	-	95
	Number Konara oaks	-	105	81
	Total	**212**	**105**	**176**

Table 2. Total ^{137}Cs inventory in three simulation cases.

Simulation	Total ^{137}Cs inventory (GBq)		
	Site A	Site B	Site C
Case 1 – with buildings and trees	147.8	138.3	65.09
Case 2 – no buildings and trees	147.0	137.9	64.60
Case 3 – no buildings and trees, ^{134}Cs and ^{137}Cs included in soil beneath building locations	163.5	155.7	75.48

Table 3. Summary of $\dot{H}^{*}(10)$ measurements averaged in 10×10 m regions, and statistics comparing case 1 simulations against measurement results.

	Site			
	A	B	C	All
Number of 10×10 m regions	67	31	42	140
Mean $\dot{H}^{*}(10)$ measurement (μSv/h)	7.0	4.9	3.7	5.6
Min $\dot{H}^{*}(10)$ measurement (μSv/h)	4.4	2.8	3.0	2.8
Max $\dot{H}^{*}(10)$ measurement (μSv/h)	11.9	8.5	5.2	11.9
Statistics comparing case 1 simulation & measurements				
Root mean square deviation (μSv/h)	1.7	2.1	0.8	1.6
Mean absolute percentage deviation (%)	21	35	18	23
Pearson correlation coefficient	0.62	0.54	0.26	0.77

Table 4. Comparison of three simulation cases. Table shows mean $\dot{H}^{*}(10)$ results over entire 160×160 m central area of each site (excluding 10×10 m tally regions predominantly inside buildings). Relative differences of results compared to the corresponding case 1 simulation are shown in the parentheses.

Simulation	Mean $\dot{H}^{*}(10)$ (μSv/h)			
	Site A	Site B	Site C	All sites
Case 1 – with buildings and trees	8.8	8.6	3.9	7.2
Case 2 – no buildings and trees	9.3 (+5.5%)	8.9 (+3.1%)	4.2 (+7.8%)	7.6 (+5.0%)
Case 3 – no buildings and trees, ^{134}Cs and ^{137}Cs included in soil beneath building locations	10.3 (+16%)	9.6 (+11%)	4.7 (+20%)	8.3 (+15%)
Simple open field calculation with mean unpaved surface ^{134}Cs and ^{137}Cs inventory (infinite half-space geometry)	12.6 (+42%)	12.6 (+46%)	6.0 (+54%)	10.6 (+48%)

Supplementary Material to Simulation study of the effects of buildings and trees on ambient dose equivalent rates outdoors at three suburban sites near Fukushima Dai-ichi

Table S1. Densities and elemental compositions of materials in PHITS models.

	Material	Density (g/cm^3)	Elemental composition (wt%)
	Air	0.012	H:0.06, C:0.01, N:75.1, O:23.6, Ar:1.3
Ground materials	Soil	Various [b]	H:2.2, O:57.5, Al:8.5, Si:26.2, Fe:5.6
	Litter in Japanese cedar forests	0.24	H:5.7, C:48.1, O:42.3, N:1.2, Na:0.05, Mg:0.2, P:0.05, Si:0.02, K:0.2, Ca:1.9, Fe:0.2
Trees	Japanese cedars and konara oaks	Various [c]	H:6.1, C:50.5, O:43.4
Building materials [a]	Construction wood	0.53	H:6.1, C:49.7, N:0.1, O:44.2
	Clay tiles	2.2	O:48.4, Na:0.8, Mg:1.1, Al:12.2, Si:29.4, K:2.0, Ca:1.9, Fe:3.7
	Concrete	2.15	H:0.4, O:50.7, Mg:0.1, Al:0.4, Si:38.6, Ca:6.9, Fe:2.9
	Glass	2.4	O:46.0, Na:9.6, Si:33.7, Ca:10.7
	Sheet metal (galvalume)	7.85	Al:3.0, Fe:91.0 Zn:6.0

[a] Material densities and compositions from Furuta and Takahashi (2015).

[b] See Tables S4, S5 and S6.

[c] See Tables S2 and S3.

Table S2. Distribution of ^{134}Cs and ^{137}Cs in Japanese cedar trees [a].

Layer	Density (g/cm^3)	Concentration (mBq/cm^3)			
		Site A		Site C	
		^{134}Cs	^{137}Cs	^{134}Cs	^{137}Cs
Leaves and branches	0.011	0.080	0.26	0.038	0.13
Bark	0.25	1.1	3.8	0.54	1.8
Wood	0.26	0.092	0.31	0.044	0.15

[a] Distribution calculated from 2014 measurement data for Japanese cedar site OT-S, Otama, Fukushima Prefecture, reported in Imamura et al. (2017a).

Table S3. Distribution of ^{134}Cs and ^{137}Cs in konara oak trees [a].

Layer	Density	Concentration (mBq/cm^3)			
	(g/cm^3)	Site B		Site C	
		^{134}Cs	^{137}Cs	^{134}Cs	^{137}Cs
Leaves and branches	0.001	0.072	0.24	0.034	0.11
Bark	0.74	250	840	120	400
Wood	0.75	160	530	76	250

[a] Distribution calculated from 2014 measurement data for konara oak forest KU1-Q, Kawauchi, Fukushima Prefecture, reported in Imamura et al. (2017a).

Table S4. Cesium-134 and ^{137}Cs concentrations as a function of depth for paved areas.

Layer	Thickness	Density	Concentration (Bq/cm^3)			
	(cm)	(g/cm^3)	Site A, B		Site C	
			^{134}Cs	^{137}Cs	^{134}Cs	^{137}Cs
1	0.1 [a]	2.4	260	890	130	420
2	9.9	1.6	0	0	0	0

[a] Inventory dispersed within 0.1 cm thick surface layer is approximation of exponential depth distribution with relaxation mass depth of 0.1 g/cm^2 (ICRU, 1994).

Table S5. Depth distribution of ^{134}Cs and ^{137}Cs in soil for unpaved areas without tall vegetation cover such as paddy fields and gardens [a].

Layer	Thickness (cm)	Density (g/cm^3)	Concentration (Bq/cm^3)			
			Site A, B		Site C	
			^{134}Cs	^{137}Cs	^{134}Cs	^{137}Cs
1	0.5	1.6	66	220	32	110
2	0.5	1.6	50	170	24	80
3	0.5	1.6	38	130	18	60
4	0.5	1.6	29	95.6	14	46
5	1.0	1.6	19	62.8	9.0	30
6	2.0	1.6	8.1	27.1	3.9	13
7	2.0	1.6	2.6	8.8	1.3	4.2
8	3.0	1.6	0.7	2.2	0.3	1.0

[a] Depth distribution is a step-wise approximation to an exponential depth distribution with relaxation mass depth 2.86 g/cm^2.

Table S6. Distribution ^{134}Cs and ^{137}Cs in litter and soil in Japanese cedar forests at sites A, C [a].

Layer	Thickness (cm)	Density (g/cm^3)	Concentration (Bq/cm^3)			
			Site A		Site C	
			^{134}Cs	^{137}Cs	^{134}Cs	^{137}Cs
Litter	0.88	0.24	23	76	11	36
Soil 1	5.0	0.24	17	57	8.2	27
Soil 2	5.0	0.35	3.4	11	1.6	5.4
Soil 3	5.0	0.40	0.9	3.1	0.4	1.5
Soil 4	5.0	0.48	0.5	1.6	0.2	0.8

[a] Distribution calculated from 2014 measurement data for Japanese cedar site OT-S (Otama, Fukushima Prefecture) reported in Imamura et al. (2017a).

Table S7. Portable Ge detector measurements of ^{137}Cs inventory on paved surfaces.

Site	Surface	^{137}Cs inventory (kBq/m^2)	Measurement date
B [a]	Paved parking area	1000	Dec. 16 2014
B [b]	Paved road	720	Dec. 18 2014
C [b]	Paved parking area	420	Dec. 17 2014

[a] Measurement of paved ground denoted site No. 2 in Yoshimura et al. (2017).

[b] Previously unpublished portable Ge detector measurements taken as per Yoshimura et al. (2017).

Table S8. Cesium-134 and ^{137}Cs inventories of different land covers, decay-corrected to January 18, 2015.

Site	Surface	^{134}Cs inventory (kBq/m^2)	^{137}Cs inventory (kBq/m^2)
A, B	Paved [a]	260	880
A, B	Unpaved and forest [b]	1300	4500
A, B	Building outer surfaces [c]	18	59
C	Paved	130	420
C	Unpaved and forest [b]	640	2100
C	Building outer surfaces [c]	8.5	28

[a] Decay-corrected mean of the two paved surface measurements at site B in Table S7.

[b] Inventory ratio of 0.18 between paved ground and unpaved permeable ground (Yoshimura et al., 2017), and decay correction.

[c] Inventory ratio of 0.012/0.18 between building outer surfaces and paved ground, where 0.012 is calculated as the average of four walls and a roof (Yoshimura et al., 2017).

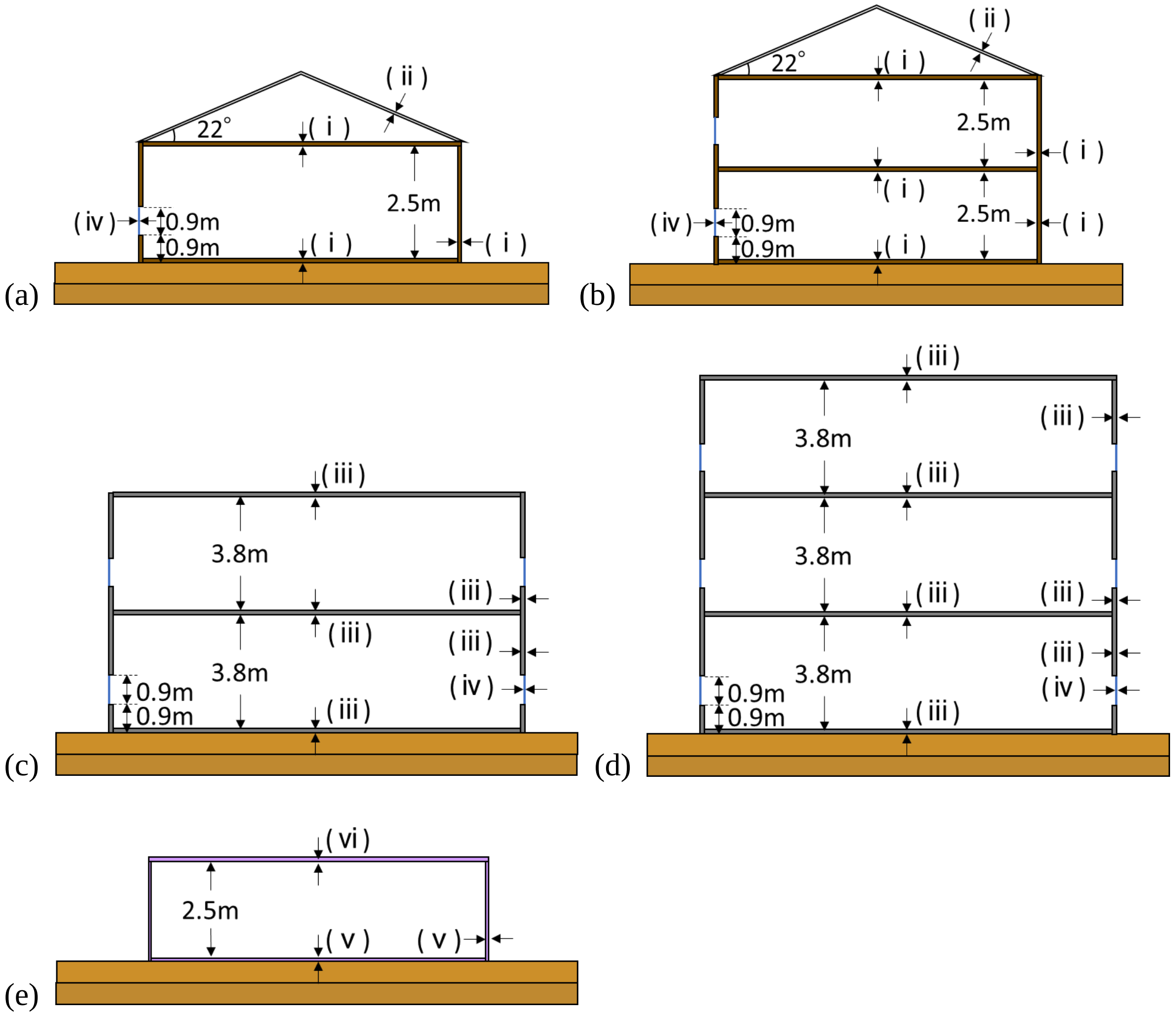

Figure S1. Models of building in the simulations: (a) wooden, single-story, (b) wooden, two-story, (c) concrete, two-story, (d) concrete, three-story, (e) sheet metal, single-story. Material thicknesses parameters are (i) 2 cm wood; (ii) 2.5 cm clay tile and 2 cm wood; (iii) 15 cm concrete; (iv) 0.4 cm glass; (v) 0.06 cm galvalume; (vi) 0.1 cm galvalume. Designs follow Furuta and Takahashi (2015).

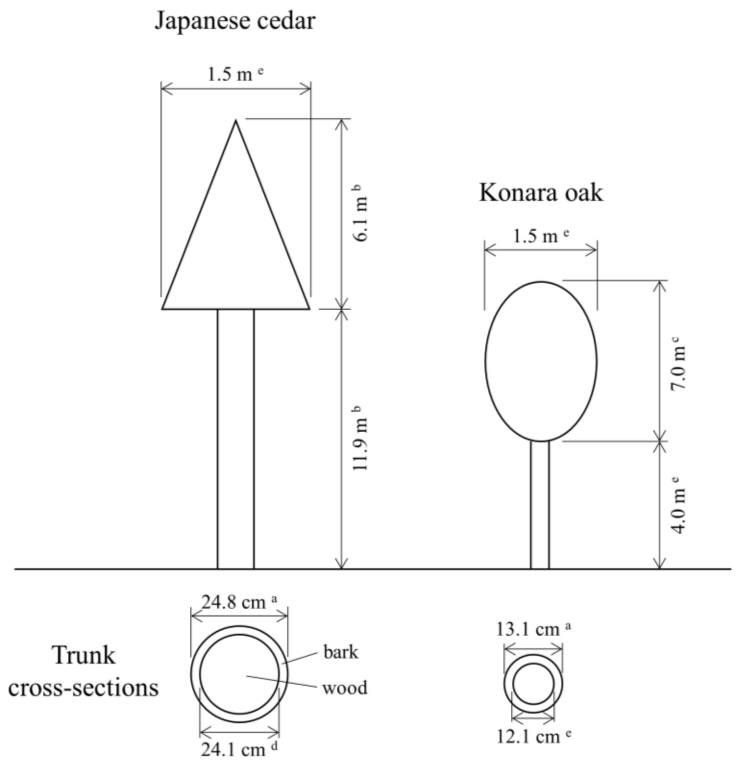

Figure S2. Models of Japanese cedar and konara oak trees. Trunks were modelled as two concentric cylinders representing bark and wood. Branches and needles of Japanese cedars were modelled as diffuse cones of organic material, whereas branches and leaves of konara oaks were modelled as ellipsoids. References for dimensions: [a] Imamura et al. (2017a), [b] Imamura et al. (2017b), [c] Ohashi et al. (2017), [d] Kajimoto et al. (2014), [e] modelling assumption.

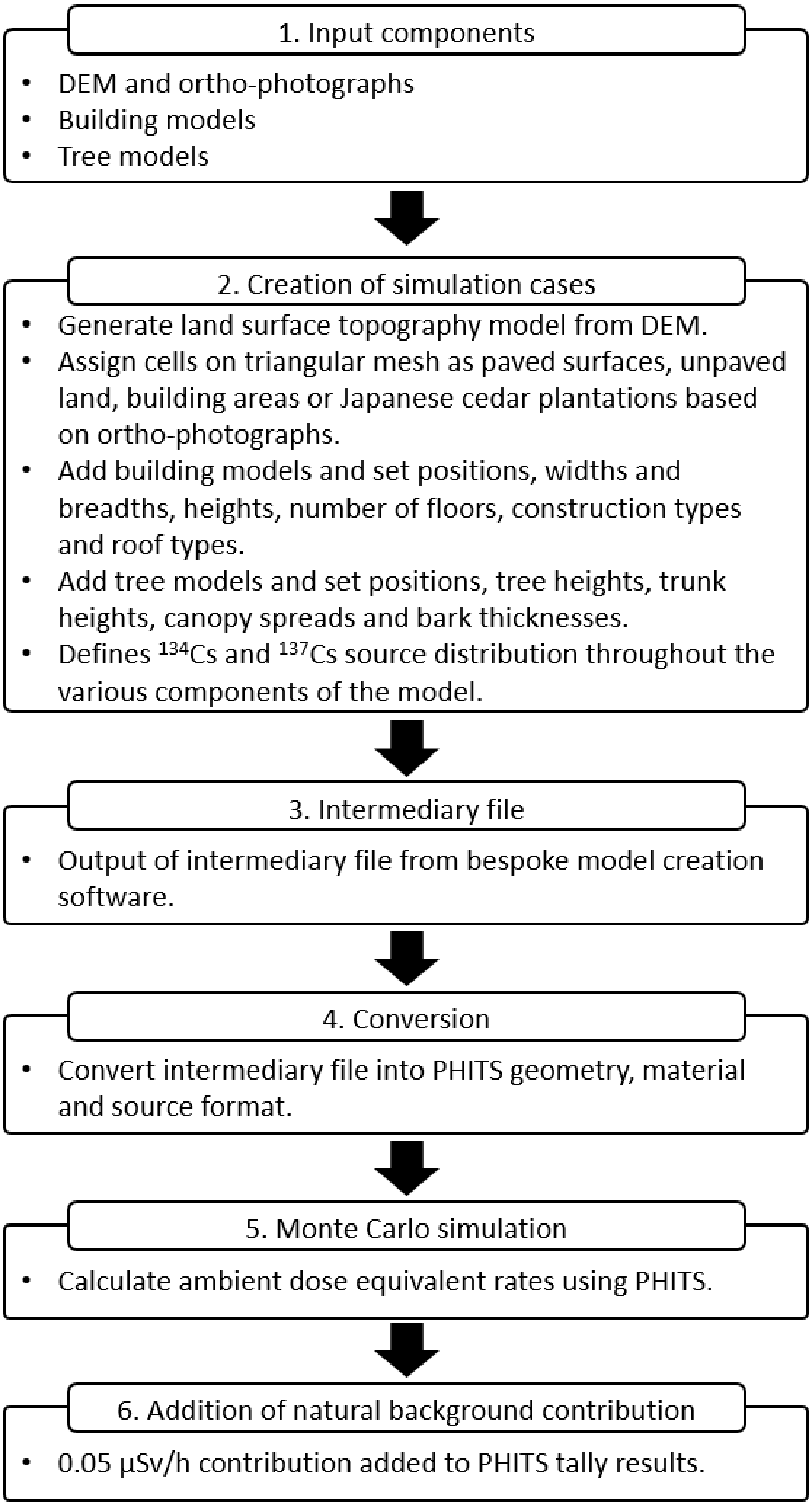

Figure S3. Block diagram showing schematic of calculation process, along with various inputs.

References

Furuta, T., Takahashi, F., 2015. Study of radiation dose reduction of buildings of different sizes and materials. J. Nucl. Sci. Technol. 52, 897-904. DOI:10.1080/00223131.2014.990939

ICRU, 1994. Gamma-ray spectrometry in the environment. ICRU Report 53.

Imamura, N., Komatsu, M., Ohashi, S., Hashimoto, S., Kajimoto, T., Kaneko S., Takano, T., 2017a. Temporal changes in the radiocesium distribution in forests over the five years after the Fukushima Daiichi Nuclear Power Plant accident. Sci. Rep. 7, 8179. DOI:10.1038/s41598-017-08261-x

Imamura, N., Akama, A., Ohtani, Y., Kobayashi, M., Tsuboyama, Y., Takahasi, M., 2017b. An estimation of air dose rate from considering of radiocesium distribution in Japanese forests. J. Jpn. For. Soc. 99, 1-9. (In Japanese) DOI:10.4005/jjfs.99.1

Kajimoto, T., Takano, T., Saito, S., Kuroda, K., Fujiwara, T., Komatsu, M., Kawasaki, T., Ohashi, S., Kiyono, Y., 2014. Methods for assessing the spatial distribution and dynamics of radiocesium in tree components in forest ecosystems. Bull. For. For. Prod. Res. Inst. 13, 113-136. (In Japanese)

Ohashi, S., Kuroda, K., Takano, T., Suzuki, Y., Fujiwara, T., Abe, H., Kagawa, A., Sugiyama, M., Kubojima, Y., Zhang, C., Yamamoto K., 2017. Temporal trends in ^{137}Cs concentrations in the bark, sapwood, heartwood, and whole wood of four tree species in Japanese forests from 2011 to 2016. J. Environ. Radioact. 178-179, 335. DOI:10.1016/j.jenvrad.2017.09.008

Yoshimura, K., Saito, K., Fujiwara, K., 2017. Distribution of ^{137}Cs on components in urban area four years after the Fukushima Dai-ichi Nuclear Power Plant accident. J. Environ. Radioact. 178-179, 48-54. DOI:10.1016/j.jenvrad.2017.07.021